Performance evaluation of an automatic MGRF-based lung segmentation approach

Ahmed Soliman, Fahmi Khalifa, and Amir AlansaryGeorgy Gimel'farbAyman El-Baz

Citation: AIP Conference Proceedings **1559**, 323 (2013); doi: 10.1063/1.4825026
View online: http://dx.doi.org/10.1063/1.4825026
View Table of Contents: http://aip.scitation.org/toc/apc/1559/1
Published by the American Institute of Physics

Performance Evaluation of an Automatic MGRF-Based Lung Segmentation Approach

Ahmed Soliman*, Fahmi Khalifa*, Amir Alansary*, Georgy Gimel'farb† and Ayman El-Baz*

*BioImaging Laboratory, Bioengineering Department, University of Louisville, Louisville, KY, USA.
†Department of Computer Science, University of Auckland, Auckland, New Zealand.

Abstract. The segmentation of the lung tissues in chest Computed Tomography (CT) images is an important step for developing any Computer-Aided Diagnostic (CAD) system for lung cancer and other pulmonary diseases. In this paper, we introduce a new framework for validating the accuracy of our developed Joint Markov-Gibbs based lung segmentation approach using 3D realistic synthetic phantoms. These phantoms are created using a 3D Generalized Gauss-Markov Random Field (GGMRF) model of voxel intensities with pairwise interaction to model the 3D appearance of the lung tissues. Then, the appearance of the generated 3D phantoms is simulated based on iterative minimization of an energy function that is based on the learned 3D-GGMRF image model. These 3D realistic phantoms can be used to evaluate the performance of any lung segmentation approach. The performance of our segmentation approach is evaluated using three metrics, namely, the Dice Similarity Coefficient (DSC), the modified Hausdorff distance, and the Average Volume Difference (AVD) between our segmentation and the ground truth. Our approach achieves mean values of 0.994 ± 0.003, 8.844 ± 2.495 mm, and 0.784 ± 0.912 mm^3, for the DSC, Hausdorff distance, and the AVD, respectively.

Keywords: Lung Segmentation, Gaussian Scale Space, Realistic Synthetic Phantoms
PACS: 87.57.nm 87.85.-d 87.85.Pq 87.57.-s 87.57.Q-

INTRODUCTION

Lung segmentation from chest Computed Tomography (CT) is a precursor to develop any Computer-Aided Diagnostic (CAD) system for lung cancer and other pulmonary diseases [1–7]. However, accurate segmentation of the lung regions from CT medical images is a challenging task, especially in the case of pathological presence (e.g., cancer, pneumonia, etc.). Since in this paper we focus on the validation of any lung segmentation approach, below we will give a short overview of some of the related work on lung segmentation. In literature, lung segmentation techniques can be classified into four main categories: 1) signal thresholding methods, 2) deformable boundary-based methods, 3) shape-based methods, and 4) edge-based methods.

Signal thresholding segments the lung and its background from chest images by analyzing an empirical probability distribution, or histogram of pixel intensities in a region-of-interest. Hu et al. [8] proposed an iterative thresholding-based technique to obtain an initial lung region. Then, morphological opening and closing operations were used to refine the obtained initial segmentation. A similar approach was developed by Ross et al. [9] using the Otsu's method [10] to segment the lung fields as a step of

2013 International Symposium on Computational Models for Life Sciences
AIP Conf. Proc. 1559, 323-332 (2013); doi: 10.1063/1.4825026

lung lobe extraction, instead of using the iterative thresholding. Ye et al. [11] used a 3D adaptive fuzzy threshold to segment the lung from CT data followed by smoothing of the segmented lung contour using 1D Gaussian.

Deformable boundaries have also been recognized as one of the most powerful segmentation methods due to its ability to produce continuous segmentation of the lung. Itai et al. [12] used a 2D parametric deformable model approach to extract lung tissues. In their framework, the deformable boundary is initialized based on a threshold estimated from CT data, and the lung borders were used as an external force to constrain the deformable model evolution. Annangi et al. [13] introduced a variational level-set approach for lung segmentation from Posterior-Anterior (PA) chest X-ray images. Their approach integrated prior shape of the lung with probabilistic edge- and region-based statistics.

Shape-based approaches have also been exploited as powerful segmentation tools, whereby priori knowledge about the lung can be integrated into the segmentation work flow. Van Ginneken et al. [14] used an optimized Active Shape Model (ASM) to segment the lung fields. They compared the segmentation with an Active Appearance Model (AAM)-based segmentation and multi-scale resolution pixel classification, concluding that the latter gives the best results. Sun et al. [15] segmented the lungs using a 3D ASM matching method and a globally optimal surface-finding method to obtain a refined and smoothed segmentation. Besbes et al. [16] used a graph-based shape model with image cues based on boosted features to segment the lung fields from chest radiographs.

Edge-based techniques have also been employed for the detection of lung region in chest CT images. For example, Campadelli et al. [17] detected an initial outline of lung borders by using the first derivative of Gaussian filters taken at four different orientations. Then, an edge tracking procedure, using the Laplacian of Gaussian (LoG) operator at three different scales, is used to find a continuous external lung contour, which is further integrated with the initial outline to produce the final lung segmentation from PA chest radiographs. Korfiatis et al. [18] used the wavelet transform to highlight lung borders in 2D stack images. An optimal threshold, selected by the minimum error criterion [19], is applied to the wavelet-processed 2D stacks to segment the lung. Finally, a morphological processing is used to refine the segmentation. For a more comprehensive review on lung segmentation, please see [20].

Most of the above methods have been validated based on a ground truth that is obtained manually by a radiologist. However, this ”gold standard" ground truth may not be accurate due to hand shaking and observer’s variability. Additionally, several studies (e.g., [21–23]) evaluated the accuracy and limitations of a number of commercial segmentation packages that have been released by CT vendors. To overcome these limitations, we introduce a validation approach that generates 3D realistic phantoms to validate our developed segmentation approach [24, 25]. To the best of our knowledge, we are the first authors who have introduced 3D realistic synthetic phantoms that simulate both appearance and 3D geometry of a real lung in order to validate segmentation approaches.

MATERIALS AND METHODS

We propose a framework to validate the accuracy of our previously developed Markov-Gibbs Random Field (MGRF)-based lung segmentation approach [24, 25]. In this paper, we will focus on the validation of our segmentation method using 3D realistic synthetic phantoms. Details of our segmentation method are fully described in [24, 25]. For completeness, a short overview of our MGRF-based segmentation approach is given below.

Joint Markov-Gibbs Model of CT Lung Images

We have previously explored a framework for the precise segmentation of lung tissues from CT images [24, 25]. Our framework describes CT images, Gaussian Scale Space (GSS) data generation using Gaussian Kernels (GKs), and desired region (binary) maps (lung and the other chest tissues), using a two-level joint MGRF image model. The latter integrates two image features, namely the first–order visual appearance of the CT images and a second–order MGRF spatial interaction model. The first-order visual appearance of lung tissues in CT data signals is described by a Linear Combination of Discrete Gaussians (LCDG) [26–28] , which is a modified version of the Linear Combination of Gaussians (LCG)-approximation of the conditional marginal signal distributions [29–31]. In addition to the LCDG-intensity model, the spatial relationships between the lung voxels are also taken into account using the popular Potts model (MGRF with the nearest 26-pixel neighborhood, see Fig. 1) with bi-valued Gibbs potentials [31].

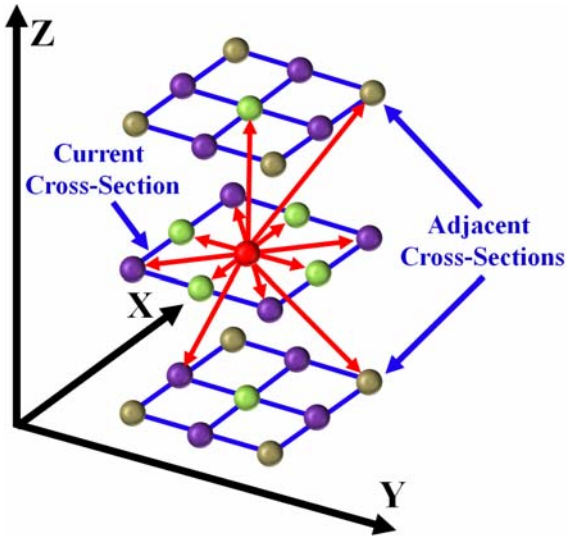

FIGURE 1. The nearest 26 voxel neighborhood.

The goal of this paper is to validate our segmentation approach. Therefore, the joint MGRF model is used to describe both the original 3D phantom images and their generated filtered GSS data. Three filtered GSS phantoms were generated from the original

3D phantom using 3D GKs as described in [24, 25]. Once the segmentations of the original phantom and its GSS data are obtained, a Bayesian approach is used to fuse results such that the final decision for each voxel to be classified as lung or background will be based on a new estimated posterior probability [32]. The developed lung segmentation framework [24, 25] is implemented to utilize both the CPU and GPU. The main steps of our lung segmentation approach are summarized in Algorithm 1. For more details, please see [24, 25, 32]

Algorithm 1 Basic Steps of Lung Segmentation Approach

- **Step 1. Input (CPU):** Read the original 3D data and generate the Gaussian filtered data in scale space by convolving the original image with the 3D GKs.
- **Step 2. Initialization (CPU):** Use marginal intensity estimated using LCDG [26–28] to get an initial map.
- **Step 3. Iterative Refinement (GPU):** Refine initial maps of original and Gaussian filtered data by iterating the following two steps:
  1. Estimate the Gibbs potential for the map **m**.
  2. Re-collect the empirical gray level densities for the current regions, re-approximate their densities, and update the map.
- **Step 4. Output (CPU):** The final map for the original and Gaussian filtered images are fused together to get the final segmentation of the lung regions using the Bayesian fusion approach [24, 25]).

Generation of the 3D Realistic Synthetic Phantoms

Since it is very difficult to obtain accurate manual segmentation of the lung tissues due to observers' variability and hand shaking, we have created realistic synthetic 3D phantoms [32] to evaluate the performance of our segmentation framework [24, 25]. The 3D phantom images were generated to mimic the visual appearance of real 3D CT data (Fig. 2) based on the integration of the Gibbs sampler and the MAP estimates for a pairwise energy function of a Generalized 3D Gauss-Markov Random Field (GGMRF) probabilistic model [33]. For completeness, basic steps for phantom generation are outlined in Algorithm 2.

PERFORMANCE EVALUATION

We use three metrics to evaluate the segmentation accuracy, specifically, the Dice Similarity Coefficient (DSC), the modified Hausdorff distance, and the Average Volume Difference (AVD) between the segmentation and the ground truth [34]. The DSC measures the similarity between the segmented and ground truth regions [34]:

$$\mathrm{DSC} = \frac{2 \cdot \mathrm{TP}}{2 \cdot \mathrm{TP} + \mathrm{FP} + \mathrm{FN}} \tag{1}$$

Algorithm 2 Main Steps of 3D Phantom Generation

- **Step 1. Initialization:** Generate an initial 3D phantom by selecting random grey level samples from real 3D CT chest data using Gibbs Sampler (Fig. 2,(A)).
- **Step 2. Energy minimization:** For each voxel of the constructed 3D phantom:
  1. Define the voxel's 26-neighborhood, N, as shown in Fig. 1.
  2. Use a gradient descent optimization algorithm to get the MAP estimate ($\widehat{q}_s$) of the grey level value (q_s) at the 3-D location $s = (i, j, z)$ using the 3D GGMRF [33]:

$$\widehat{q}_s = \arg\min_{\widetilde{q}_s} \left\{ |q_s - \widetilde{q}_s|^{\alpha} + \rho^{\alpha}\lambda^{\beta} \sum_{r \in N} \eta_{s,r} \, |\widetilde{q}_s - q_r|^{\beta} \right\}$$

  where $\eta_{s,r}$ is the GGMRF potential, and ρ and λ are scaling factors. The parameter $\beta \in [1.01, 2.0]$ controls the level of smoothing (e.g., smooth, $\beta = 2$, vs. relatively abrupt edges, $\beta = 1.01$). The parameter $\alpha \in \{1, 2\}$ determines the Gaussian, $\alpha = 2$, or Laplace, $\alpha = 1$, prior distribution of the estimator.
- **Step 3. Estimation refinement:** Iterate step 2 until there is no change in the estimated grey level value.

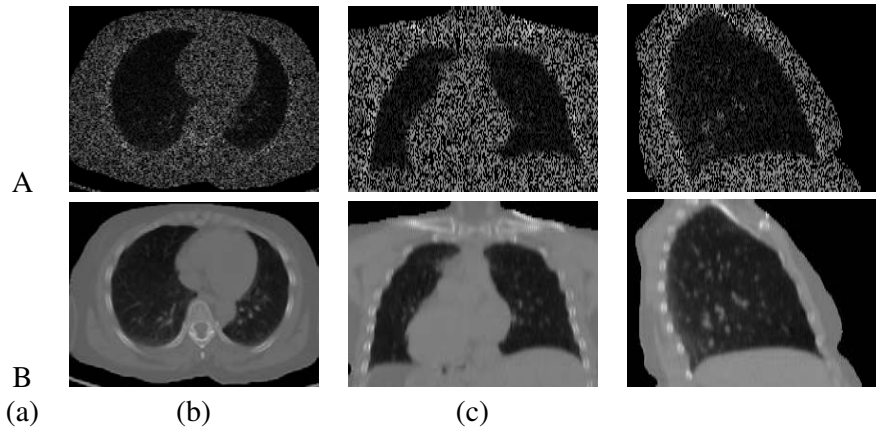

FIGURE 2. A typical realistic 3D phantom: initialization (A) and final phantom (B) projected on to axial (a), coronal (b), and sagittal (c) planes for visualization. This phantom was generated using the following parameters: $\rho = 1$, $\lambda = 5$, $\beta = 1.01$, $\alpha = 2$, and $\eta_{s,r} = \sqrt{2}$.

where TP, FP, and FN stand for the True Positive, False Positive, and False Negative segmentation results, respectively (see Fig. 3). For a segmented region, **SR**, and its ground truth, **GT**, TP $= |\mathbf{SR} \cap \mathbf{GT}|$ is the area of their overlap, i.e., the number of the common points in **SR** and **GT**; FP $= |\mathbf{SR} - \mathbf{SR} \cap \mathbf{GT}|$ is the number of points in the difference between **SR** and TP, and FN $= |\mathbf{GT} - \mathbf{SR} \cap \mathbf{GT}|$ is the number of points in the difference between **GT** and TP. The closer the DSC to "1", the better the segmentation.

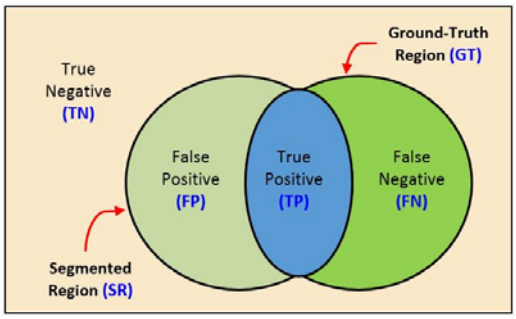

FIGURE 3. Schematic illustration for the determination of the Dice Similarity Coefficient (DSC).

Another metric, which is used to evaluate the segmentation accuracy, is the Hausdorff distance. Hausdorff distance from a set $\mathbf{A_1}$ to a set $\mathbf{A_2}$ is defined as the maximum distance of the set $\mathbf{A_1}$ to the nearest point in the set $\mathbf{A_2}$ [34]:

$$H(\mathbf{A_1},\mathbf{A_2}) = \max_{c\in\mathbf{A_1}}\{\min_{e\in\mathbf{A2}}\{d(c,e)\}\} \tag{2}$$

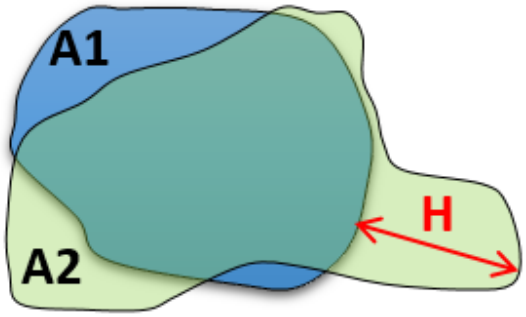

FIGURE 4. Schematic diagram for the determination of the Hausdorff Distance.

where c and e are points of sets $\mathbf{A_1}$ and $\mathbf{A_2}$, respectively, and $d(c,e)$ is Euclidean distance between these points. The bidirectional Hausdorff distance, $H_{\mathrm{Bi}}(\mathbf{GT},\mathbf{SR})$, between the segmented region **SR** and its ground truth **GT** is defined as: $H_{\mathrm{Bi}}(\mathbf{GT},\mathbf{SR}) = \max\{H(\mathbf{GT},\mathbf{SR}),H(\mathbf{SR},\mathbf{GT})\}$. In this paper, we used the 95-percentile bidirectional modified Hausdorff distance as a metric that measures the segmentation accuracy. The smaller the distance, the better the segmentation. The ideal case with perfect segmentation is when the bidirectional Hausdorff distance is equal to 0. In addition to the DSC and MHD metrics, a volumetric metric is used to assess the accuracy of the segmentation. The AVD is calculated between the segmentation and the ground truth and is used to test the segmentation accuracy. The smaller the volume difference, the better the segmentation.

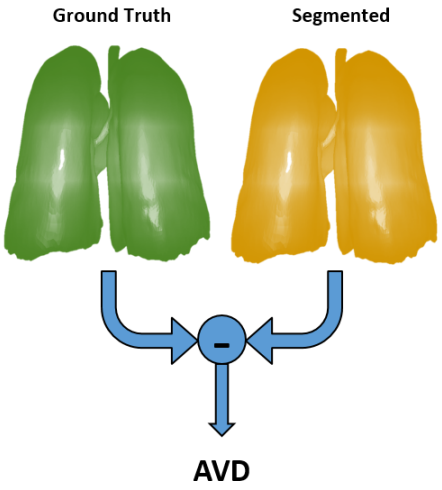

FIGURE 5. Illustration for the measurement of the Average Volume Difference (AVD) metric between the segmented and ground truth volumes.

EXPERIMENTAL RESULTS AND CONCLUSIONS

We used Algorithm 2 to simulate 3D realistic phantoms with the same scanning parameters of the data we had [24], so the size of each 3D realistic phantom is $512 \times 512 \times 390$. Experimental results are acquired by running Algorithm 1 on both CPU and GPU/CUDA. Regarding the CPU implementation, the algorithm is tested on a platform with 3.33 Intel Xeon CPU, and 48 GB RAM. All the GPU implementations are executed on an NVIDIA Tesla C1060 GPU card installed on a Linux machine with a 3.3 GHz Intel Xeon CPU and 48 GB RAM.

To test the accuracy of the developed segmentation approach, we generated five independent 3D lung phantoms. Then, our segmentation method [24, 25] was applied to the constructed phantoms to extract the lung tissue. Segmentation results for three phantoms are shown in Fig. 6. The agreement between our automated segmentation results and the manually contoured ground truth is assessed using the Dice Similarity Coefficient (DSC), modified Hausdorff Distance (MHD), and the Average Volume Difference (AVD) metrics, as defined above in Section . Table 1 summarizes the statistics for the DSC, MHD, and AVD metrics obtained using our segmentation approach for all phantoms.

In conclusion, this paper introduces a new framework to generate 3D realistic synthetic phantoms that have the same geometry and appearance of real lung data. The generated phantoms can be used to evaluate the performance of any lung segmentation approach. The framework models the 3D appearance of the lung tissue based on using 3D GGMRF of voxel intensities with pairwise interaction. Then, the learned 3D-GGMRF image model is used to iteratively minimize the energy function to simulate the appearance of the generated 3D phantoms. The phantoms were subsequently used to validate our developed Joint Markov-Gibbs based lung segmentation approach.

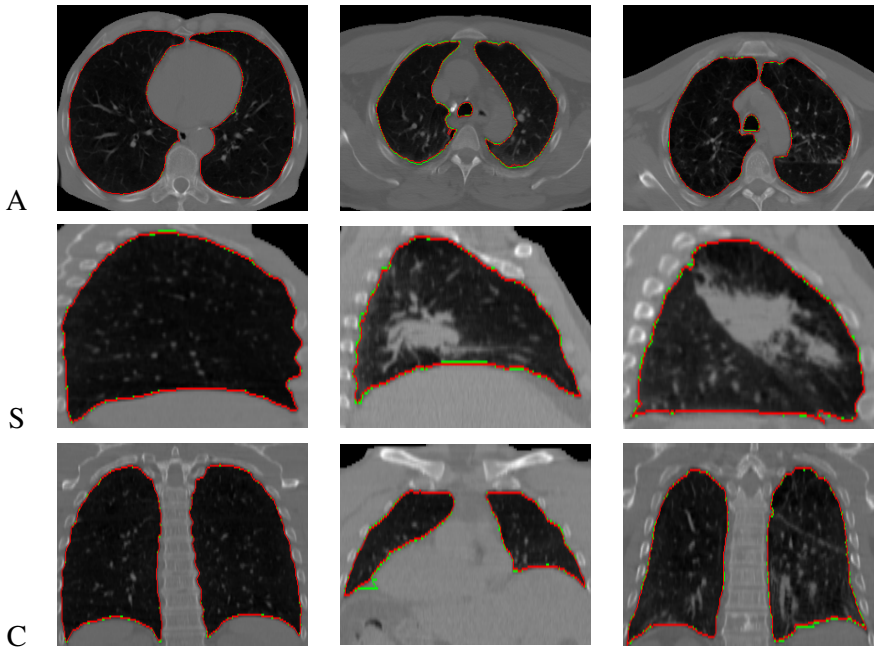

FIGURE 6. Results of 3D lung segmentation projected onto 2D axial (A), sagittal (S), and coronal (C) planes for visualization for three different CT data, (a), (b), and (c). The model segmentation and ground truth contours are shown in red and green, respectively.

TABLE 1. Accuracy of our segmentation approach using the Dice, Hausdorff distance, and average volume difference metrics. Note that "STD", "DSC", "MHD", and "AVD" stand for standard deviation, Dice similarity coefficient, modified Hausdorff distance, and average volume difference, respectively.

	Evaluation Metric		
	DSC	MHD (in mm)	AVD (in mm^3)
Min.	0.988	5.042	0.029
Max.	0.996	12.00	2.372
Mean	0.994	8.844	0.784
STD	0.003	2.495	0.912

ACKNOWLEDGMENTS

This research work has been supported by Research Scholar Grants, 120556-RSG-11-266-01-CCE, from the American Cancer Society.

REFERENCES

1. A. El-Baz, A. A. Farag, R. Falk, and R. La Rocca, “Detection, visualization and identification of lung abnormalities in chest spiral CT scan: Phase-I," In *Proc. International Conference on Biomedical Engineering (ICBE’02)*, Cairo, Egypt, December 24–25, 2002, pp. 38–42.
2. A. El-Baz, A. A. Farag, R. Falk, and R. La Rocca, “A unified approach for detection, visualization, and identification of lung abnormalities in chest spiral CT scans," *International Congress Series*, vol. 1256, pp. 998–1004, 2003.
3. A. A. Farag, A. El-Baz, G. Gimel’farb, and R. Falk, “Detection and recognition of lung abnormalities using deformable templates," In *Proc. International Conference on Pattern Recognition (ICPR’04)*, Cambridge, UK.m August 23–26, 2004, vol. 3, pp. 738–741.
4. A. A. Farag, A. El-Baz, G. Gimel’farb, M. A. El-Ghar, and T. Eldiasty, “Quantitative nodule detection in low dose chest CT scans: new template modeling and evaluation for CAD system design," In *Proc. International Conference on Medical Image Computing and Computer-Assisted Intervention (MICCAI’05)*, Palm Springs, CA, USA, October 26–29, 2005, pp. 720–728.
5. A. Farag, A. El-Baz, G. Gimel’farb, R. Falk, M. A. El-Ghar, T. Eldiasty, and S. Elshazly, “Appearance models for robust segmentation of pulmonary nodules in 3D LDCT chest images," In *Proc. International Conference on Medical Image Computing and Computer-Assisted Intervention (MICCAI’06)*, Copenhagen, Denmark, October 1–6, 2006, pp. 821–829.
6. A. El-Baz, G. Gimel’farb, R. Falk, and M. Abo El-Ghar, “Automatic analysis of 3D low dose ct images for early diagnosis of lung cancer," *Pattern Recognition Journal*, vol. 42, no. 6, pp. 1041–1051, 2009.
7. A. El-Baz, A. Elnakib, M. Abou El-Ghar, G. L. Gimel’farb, R. Falk, A. A. Farag, “Automatic detection of 2D and 3D lung nodules in chest spiral CT scans," *International Journal of Biomedical Imaging*, vol. 2013, pp. 1–11, 2013.
8. S. Hu, E. Hoffman, and J. Reinhardt, “Automatic lung segmentation for accurate quantitation of volumetric X-ray CT images," *IEEE Transactions on Medical Imaging*, vol. 20, pp. 490–498, 2001.
9. J. C. Ross, R. S. J. Estépar, A. Díaz, C.-F. Westin, R. Kikinis, E. K. Silverman, and G. R. Washko, “Lung extraction, lobe segmentation and hierarchical region assessment for quantitative analysis on high resolution computed tomography images," In *Proc. International Conference on Medical Image Computing Computer-Assisted Intervention (MICCAI’09)*, London, UK, September 20–24, 2009, pp. 690–698.
10. N. Otsu, "A threshold selection method from gray-level histograms," *IEEE Transactions on Systems Man Cybernetics*, vol. 9, no. 1, pp. 62–66, 1979.
11. X. Ye, X. Lin, J. Dehmeshki, G. Slabaugh, and G. Beddoe, “Shape-based computer-aided detection of lung nodules in thoracic CT images," *IEEE Transactions on Biomedical Engineering*, vol. 56, no. 7, pp. 1810–1820, 2009.
12. Y. Itai, K. Hyoungseop, S. Ishikawa, S. Katsuragawa, T. Ishida, K. Nakamura, and A. Yamamoto, “Automatic segmentation of lung areas based on SNAKES and extraction of abnormal areas," In *Proc. IEEE International Conference on Tools with Artifitial Intelligence (ICTAI’05)*, Hong Kong, China, November 14–16, 2005, pp. 377–381.
13. P. Annangi, S. Thiruvenkadam, A. Raja, H. Xu, X. Sun, and L. Mao, “A region based active contour method for X-ray lung segmentation using prior shape and low-level features," In *Proc. International Symposium on Biomedical Imaging: From Nano to Macro (ISBI’10)*, Rotterdam, The Netherlands, April 14–17, 2010, pp. 892–895.
14. B. van Ginneken, M. B. Stegmann, and M. Loog, “Segmentation of anatomical structures in chest radiographs using supervised methods: A comparative study on a public database," *Medical Image Analysis*, vol. 10, no. 1, pp. 19–40, 2006.
15. S. Sun, C. Bauer, and R. Beichel, “Automated 3-D Segmentation of lungs with lung cancer in CT data using a novel robust active shape model approach," *IEEE Transactions on Medical Imaging*, vol. 31, no. 2, pp. 449–460, 2012.
16. A. Besbes and N. Paragios, “Landmark-based segmentation of lungs while handling partial correspondences using sparse graph-based priors," In *Proc. International Symposium on Biomedical Imaging: From Nano to Macro, (ISBI’11)*, Chicago, Illinois, USA, March 30 - April 2, 2011, pp. 989–995.
17. P. Campadelli, E. Casiraghi, and D. Artioli, “A fully automated method for lung nodule detection

from postero-anterior chest radiographs," *IEEE Transactions on Medical Imaging*, vol. 25, no. 12, pp. 1588–1603, 2006.
18. P. Korfiatis, S. Skiadopoulos, P. Sakellaropoulos, C. Kalogeropoulou, and L. Costaridou, "Combining 2D wavelet edge highlighting and 3D thresholding for lung segmentation in thin-slice CT," *British Journal of Radiology*, vol. 80, no. 960, pp. 996–1004, 2007.
19. J. Kittler, and J. Illingworth, "Minimum error thresholding," *Pattern Recognition*, vol. 19, no. 1, pp. 41–47, 1986.
20. A. El-Baz, G. M. Beache, G. Gimel'farb, K. Suzuki, K. Okada, A. Elnakib, A. Soliman, and B. Abdollahi, "Computer-aided diagnosis systems for lung cancer: Challenges and methodologies," *International Journal of Biomedical Imaging*, vol. 2013, pp.1 46, 2013.
21. D. Wormanns, G. Kohl, E. Klotz, A. Marheine, F. Beyer, W. Heindel, and S. Diederich, "Volumetric measurements of pulmonary nodules at multi-row detector CT: In vivo reproducibility," *European Radiology*, vol. 14, no. 1, pp. 86–92, 2004.
22. S. G.Jennings, H. T. Winer-Muram, M. Tann, J. Ying, and I. Dowdeswell, "Distribution of stage I lung cancer growth rates determined with serial volumetric CT measurements," *Radiology*, vol. 241, no. 2, pp. 554–563, 2006.
23. A. El-Baz, P. Sethu, G. Gimel'farb, F. Khalifa, A. Elnakib, R. Falk, and M. Abu El-Ghar, "Elastic phantoms generated by microfluidics technology: Validation of an imaged-based approach for accurate measurement of the growth rate of lung nodules," *Biotechnology Journal*, vol. 6, no. 2, pp. 195–203, 2011.
24. B. Abdollahi, A. Soliman, C. Civelek, X. Li, G. Gimel'farb, and A. El-Baz, "A novel Gaussian scale-space based-joint MGRF framework for precise lung segmentation," In *Proc. International Conference on Image Processing, ICIP'12*, Orlando, Florida, USA, September 30 Ű- October 3, 2012, pp. 2029–2032.
25. B. Abdollahi, A. Soliman, C. Civelek, X. Li, G. Gimel'farb, and A. El-Baz, "A novel 3D joint MGRF framework for precise lung segmentation," In *Proc. Machine Learning in Medical Imaging (MLMI'12)*, Nice, France, October 1, vol. 7588, pp. 86–93, 2012.
26. A. El-Baz, and G. Gimel'farb, "EM based approximation of empirical distributions with linear combinations of discrete Gaussians," In *Proc. International Conference on Image Processing, ICIP'07*, San Antonio, Texas, USA, September 16–19, 2007, pp. 373–376.
27. A. El-Baz, A. Elnakib, F. Khalifa, M. Abou El-Ghar, P. McClure, A. Soliman, and G. Gimel'farb, "Precise segmentation of 3-D magnetic resonance angiography," *IEEE Transactions on Biomedical Engineering*, vol. 59, no. 7, pp. 2019–2029, 2012.
28. A. El-Baz, Novel stochastic models for medical image analysis, Ph.D. dissertation, University of Louisville, Louisville, KY, USA, 2006.
29. A. Farag, A. El-Baz, and G. Gimel'farb, "Density estimation using modified expectation maximization for a linear combination of Gaussians," In *Proc. International Conference on Image Processing (ICIP'04)*, Singapore, October 24–27, 2004, vol. III, pp. 1871–1874.
30. G. Gimel'farb, A. Farag, and A. El-Baz, "Expectation-Maximization for a Linear Combination of Gaussians," In *Proc. International Conference on Pattern Recognition (ICPR'04)*, Cambridge, UK, August 23-Ű26, 2004, vol. III, pp. 422-Ű425
31. A. Farag, A. El-Baz, and G. Gimelfarb, "Precise segmentation of multi-modal images," *IEEE Transactions on Image Processing*, vol. 15, no. 4, pp. 952–968, 2006.
32. A. Soliman, F. Khalifa, A. Alansary, G. Gimel'farb, and A. El-Baz, "Segmentation of lung region based on using parallel implementation of joint MGRF: Validation on 3D realistic lung phantoms," In *Proc. International Symposium on Biomedical Imaging: From Nano to Macro, (ISBI'13)*, San Francisco, CA, USA, 2013, April 7-11, pp. 852–855.
33. C. Bouman and K. Sauer, "A generalized Gaussian image model for edge-preserving MAP estimation," *IEEE Transactions on Image Processing*, vol. 2, no. 3, pp. 296–310, 1993.
34. K. O. Babalola, B. Patenaude, P. Aljabar, J. Schnabel, D. Kennedy, W. Crum, S. Smith, T. Cootes, M. Jenkinson, and D. Rueckert, "An Evaluation of four automatic methods of segmenting the subcortical structures in the Brain," *Neuroimage*, vol. 47, no. 4, pp. 1435–1447, 2009.